

Fluidic Control of an Aggressive Offset Diffuser for a Supersonic Inlet

Travis J. Burrows¹, Bojan Vukasinovic² and Ari Glezer³
*Woodruff School of Mechanical Engineering,
 Georgia Institute of Technology, Atlanta, GA 30332-0405*

Abstract

Losses and flow distortions in a supersonic-inlet aggressive offset diffuser ($M_{\text{throat}} < 0.64$) that are induced by closed, separated flow domains on the diffuser's concave surfaces and by pairs of dynamically coupled counter-rotating streamwise vortices are mitigated using fluidic actuation. While pressure recovery is primarily limited by the separation in each of the diffuser's turns, the distortion is governed by counter-rotating streamwise vortices that advect low-momentum fluid from the wall region into the core flow. The present investigations have shown that the secondary vortices are engendered by concentrations of streamwise vorticity that form in the outboard segments of the separated flow domains. Therefore, fluidic control of the scale and topology of the trapped vorticity within the internally-separated flow can be leveraged to control the structure and strength of the ensuing secondary vortices and thereby significantly reduce flow distortion and losses. In the present investigations, fluidic control is effected by a spanwise array of oscillating jets that are placed just upstream of the separation domain. The actuation alters the spacing and diminishes the strength of the base flow streamwise vortices by forming and adjoining streamwise vorticity concentrations of opposite sense. The spanwise distribution of the actuator array can be optimized to reduce the average circumferential distortion by as much as 60% at actuation to diffuser mass flow rate ratio of 0.4%.

Nomenclature

AIP	aerodynamic interface plane	p	static pressure
C_p	pressure coefficient	p_t	total pressure
C_q	jet mass flow rate coefficient	ξ	streamwise vorticity
D	diffuser AIP diameter	f	frequency
$DPCP_{\text{avg}}$	average SAE circumferential distortion descriptor	H	diffuser inlet height
$DPCP_h$	hub SAE circumferential distortion descriptor	I	PSP light intensity
$DPCP_t$	tip SAE circumferential distortion descriptor	L	diffuser length
$DPRP_h$	hub SAE radial distortion descriptor	M_{AIP}	AIP Mach number
$DPRP_t$	tip SAE radial distortion descriptor	M_t	throat Mach number
n	number of active jets		

¹ Graduate Research Assistant, AIAA Member.

² Research Engineer, AIAA Member.

³ Professor, Fellow AIAA.

I. Technical Background

The significant design changes in inlet systems of fighter aircraft in recent decades have underscored the increasing need for more compact, offset systems to enable inlet/airframe integration with the forebody or wings of advanced designs. However, the realization of such compact inlet systems having complex inlet apertures and highly-offset or serpentine-shaped diffusers poses significant flow management challenges that are manifested by formation of intense streamwise vortices at the cowl lips, embedded transonic shock waves at the throats, and secondary flows, possibly coupled with separation at the duct bends. These secondary-flow structures cause significant total pressure losses and flow distortion, thereby posing severe challenges for turbine-engine operability and aeromechanical response of fan blades, which can compromise the engine-compression system. Passive and active flow control technologies have offered unique potential for management of complex flows within integrated inlets, and mitigation of their adverse effects on propulsion-system performance.

Although successful applications of passive flow-control techniques for mitigation of AIP total-pressure recovery losses and distortion have been reported by a number of earlier investigators (e.g., Vakili et al. 1985, Reichert and Wendt 1996, Jirásek 2006, and Owens et al. 2008), these actuation approaches lack adjustability and result in total pressure losses. In a numerical study, Anderson and Gibb (1993) showed that an optimization of a row of vane type vortex generators in an S-duct diffuser reduced the AIP distortion (DC60 parameter) by up to 90%, by eliminating flow separation and suppressing secondary flows. Optimization work by Jirásek (2006) on complex, highly offset diffusers further corroborated the efficacy of sub-boundary layer vane actuators, where optimized configurations yielded DC60 distortion below 10% and about 2% increase in recovery at the throat Mach of 0.66. Tournier and Paduano (2005) studied an emulated thick-boundary-layer ingesting diffuser at throat Mach numbers up to 0.8, and reported that vane-type vortex generators could recover $DPCP_{avg}$ parameter below 0.05 with modest pressure recovery improvements. Owens et al. (2008) used a single vortex generator row in an S-duct diffuser at $M = 0.85$ resulting in a reduction of $DPCP_{avg}$ at the AIP below the targeted level of 0.02 for most inlet mass flow ratios.

Active flow control (AFC) approaches can lead to significant improvement in performance of offset diffusers, with potential for rapid actuation and little or no drag penalty when inactive. Application of AFC enables optimization and in-flight performance control both in the absence (Weigl et al. 1997, Scribber et al. 2006, Anderson et al. 2004) and presence (Vaccaro et al. 2008, Rabe 2003) of flow separation. Anderson et al. (2004) were concerned with suppression of engine-face distortion (through DC60) in an offset diffuser at throat $M = 0.7$ by optimization of skewed jets, and showed acceptable levels of distortion at 0.5% engine mass flow rate fraction needed for the control jets. Scribber et al. (2006) used vortex-generating jets in an offset diffuser with internal separation at $M = 0.55$ and showed reduction of peak circumferential distortion by about 70% and about 2% increase in recovery at cruise conditions. In similar experiments, Owens et al. (2008) used various arrays of vortex-generating jets in a S-duct diffuser at $M = 0.85$ to reduce average circumferential distortion below 0.02, which required total jet mass flow rate fractions higher than 2% of the engine mass flow rate. Gartner and Amitay (2015) experimentally tested the effect of sweeping, pulsed, and two-dimensional jet actuators on the pressure recovery of a rectangular diffuser under transonic flow conditions, and showed that the sweeping jets produced higher pressure recovery at comparable mass flow rates.

Hybrid control approach, that incorporates the advantages of both passive and active control, has been shown to be effective for reduction of parasitic drag while maintaining some degree of fail-safe performance, and satisfying the need for adjustable flow control. Owens et al. (2008) combined active and passive flow control by using micro-vanes and jets, and were able to suppress $DPCP_{avg}$ below 0.02 at only 0.4% fraction of the engine mass flow rate supplied to the jets. In another effort to reduce engine bleed, Anderson et al. (2009) combined the micro-ramps used in their earlier work (2006) with flow injection resulting in an almost 10-fold reduction in required engine bleed for the same level of performance.

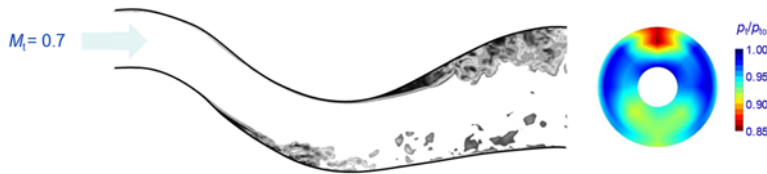


Figure 1. Schematic of the offset diffuser flow separation and measured AIP total pressure distortion.

Harrison et al. (2013) simulated, and experimentally verified, the favorable superposition of ejector-pump-like suction and blowing for a thick-boundary-layer ingesting serpentine diffuser at $M \approx 0.85$. They found that a 50% reduction of total-pressure distortion (as measured by DC60) by using a circumferential blowing scheme can be increased up to 75% in the hybrid configuration. In a more recent joint experimental-CFD investigation under NASA's Subsonic Fixed Wing Program, Boeing and Georgia Tech demonstrated the utility of hybrid (microvanes/synthetic jets) and active (synthetic jets) flow control to mitigate distortion in an offset diffuser ($L/D = 1.7$). Gissen et al. (2014a) showed that independent active and passive control approaches induced about the same reduction in the average circumferential distortion, while the application of hybrid (passive and active) control led to stronger effects on the pressure distribution at the AIP and a 35% reduction in distortion compared to the base flow. Subsequently, Gissen et al. (2014b) analyzed some time-dependent aspects of the passive and active flow control elements of the hybrid configuration. They isolated the two dominant modes that induce time-dependent reduction of the flow distortion in the presence of active/hybrid flow control. These modes are associated with the formation of two large-scale vortical structures that are formed by the merging of arrays of small-scale actuation vortices. Recently, Burrows et al. (2016) demonstrated experimentally that active flow control can alter the strength, scale, and structural topology of trapped vorticity (that was deliberately engendered in the diffuser flow) and consequently its interactions with the cross-flow, leading to significant reduction in the overall flow distortion at the AIP (up to about 80% at $M = 0.7$ and actuation mass flow rate ratio $C_q < 0.7\%$). In a subsequent joint experimental and numerical study, Vukasinovic et al. (2017) showed that further optimization of the same flow control approach can yield a reduction of about 68% in distortion at C_q as low as 0.25%.

The present investigations focus on flow management within an aggressive, three-dimensional serpentine diffuser as illustrated schematically in Figure 1. Two major sources of the flow losses and distortion are caused by local flow separation at each of the diffuser's bends on the upstream lower and downstream upper surfaces. These separation domains result in clear cross-sectional distortions of the total pressure at the aerodynamic-interface plane (AIP) showing broad, diffused total pressure deficit along the bottom surface and high, more focused deficit along the upper surface that result from the separation domains at the first and second bends, respectively. The present investigation demonstrates the utility of active flow control based on a spanwise array of fluidic oscillator jets for the mitigation of flow distortion and recovery by controlling the separation at the second turn bend.

II. Experimental Setup and Diagnostics Techniques

The present experiments are performed in a small, open-return, pull-down, high-speed subsonic wind tunnel driven by a 150 HP blower in which the temperature of the return air is controlled using a chiller, coupled with an ultra-low pressure drop heat exchanger. An aggressive offset diffuser model is installed in the tunnel such that the tunnel inlet contraction smoothly transitions to the diffuser throat (Figure 2). The diffuser has a D-shaped inlet and a round aerodynamic interface plane (AIP) with a diameter, $D = D_{AIP} = 0.127$ m, and throat Mach number up to 0.69 can be realized. The offset between the throat and AIP is $0.4 \cdot D$, length-to-diameter ratio $L/D = 3.7$, throat width $W/D = 1.78$, and throat height $H/D = 0.48$. A flow control module is integrated into diffuser design over the upper downstream surface that triggers the major flow distortion, and can accommodate active flow control elements. In addition, several optical access ports are also integrated into diffuser moldline to be utilized for flow diagnostic techniques.

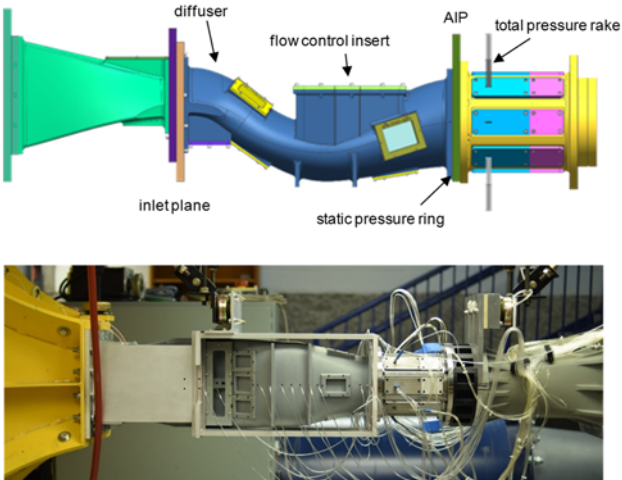


Figure 2. CAD model of the offset diffuser and a picture of the wind tunnel installation.

The main flow diagnostic equipment integrated into the diffuser includes a standard total pressure rake to measure the flow distortion at the AIP according to the industry standard ARP1420b, using 40 probes in eight, equiangular spaced rakes around the circumference of the AIP (Figure 2). The AIP total pressure rake is supplemented with a matching ring of eight static pressure ports along the diffuser wall, at the base of each rake leg. In addition, ten and thirteen static pressure ports are distributed along the bottom and top sides of the diffuser wall, respectively. Static and total pressures are measured using a dedicated PSI Netscanner system such that each set of pressure measurements is averaged over sixty-four independent samples, while the mean static and total pressures are based on 100 such sets (the uncertainty of the mean pressure is estimated to be less than 1%). The uncertainty of the derived $DPCP_{avg}$ parameter is estimated to be less than 2%. In addition to the static and total pressure measurements, pressure sensitive paint measurements and localized visualization of the flow across the control surface are utilized to elucidate the wall flow structure and shed light on the global flow topology.

Pressure sensitive paint (PSP) measurements, based on molecular photoluminescence (Liu 1997), are conducted over the flow control module installed in the second turn of the diffuser yielding spatial distribution of the static pressure over the flow control insert (capturing the central separation domain and the outboard spanwise attached domain). In this experimental technique that was developed in the 1980s and 90s (Peterson and Fitzgerald 1980, Kavandi et al. 1990) and later refined by Liu and Campbell (1997), and Bell (2001), the illuminated paint absorbs and emits light proportional to oxygen or thermal quenching at the surface. The thermal bias is typically compensated for through a second component of the paint that is only sensitive to temperature (TSP), where, in principle, both the PSP and TSP components have identical temperature sensitivity such that the paint/surface pressure ratio is related to the PSP and TSP intensity ratios as: $(I_{P,o}/I_P) \cdot (I_T/I_{T,o}) = A + B(p/p_o)$ (Bell et al. 2001, Khalil et al. 2004), where the subscripts P and T refer to the intensities of the PSP and TSP components and the coefficients A and B have to be determined experimentally through calibration. The paint is illuminated using a UV (400 nm) LED array, and the fluorescence is captured through an optical access port using a miniature CCD camera integrated into the diffuser's wall opposite to the flow control module (Figure 3a). Using the ambient conditions as a reference, the light intensity is measured simultaneously with the static pressure at eight distributed ports over a range of flow rates through the diffuser. These measurements result in the calibration curve that relates the

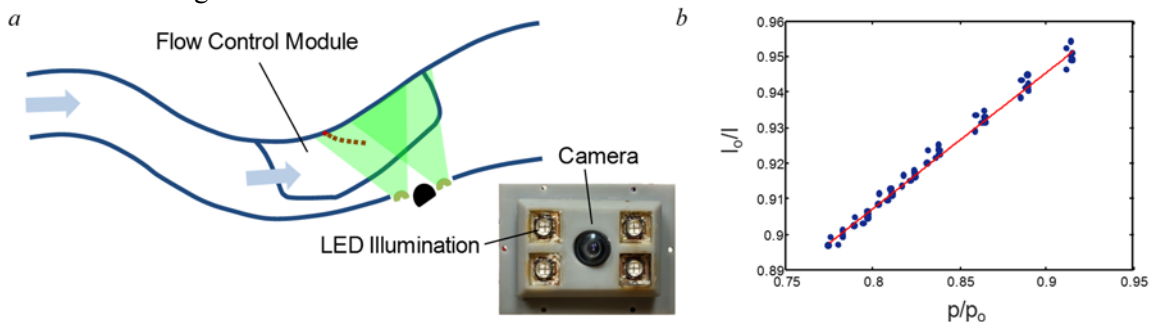


Figure 3. Schematics of the PSP diagnostics in the diffuser and a picture of the integrated components (a), and PSP intensity calibration (b).

collected light intensity ratio I_o/I and p/p_o (Figure 3b) that is used for conversion of the measured light intensity ratios into surface pressure distributions.

The diffuser characteristic Mach numbers relative to the upstream reference pressure p_{ref} were also calibrated. In one set of measurements, diffuser Mach number at the throat M_t was measured by the pitot probe centered at the throat cross-sectional area, while in the other calibration, Mach number at the AIP M_{AIP} was based on the mean rake AIP total pressure and the corresponding mean wall static pressure, each for a range of flow rates. The two resulting calibration curves are shown in Figure 4, indicating a range of the diffuser flows up to about $M_t = 0.69$. A nominal operating Mach number is based on the diffuser design requirements, and is set to $M_t = 0.64$ ($M_{AIP} = 0.53$).

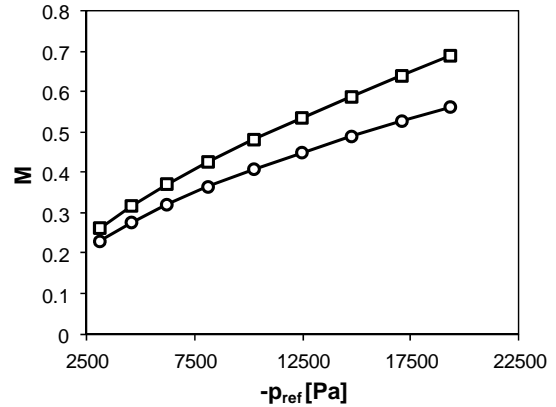


Figure 4. Variation of the diffuser throat (\square) and AIP (\circ) Mach number with reference pressure.

A spanwise array of 17 equally-spaced (6.3 mm apart) fluidic oscillating jets (similar to the array of Burrows et al., 2016), is located upstream of separation (as determined by surface oil visualization) in the second turn (Figure 5a). Each jet orifice measures 1.5×2 mm, with an operating frequency between $f = 7 - 9$ kHz over a range of flow rates. The flow control jets are designed to blow at an angle of 55° relative to the streamwise direction and half the array on each side of the spanwise centerline is skewed towards the sidewall of the duct (cf. Figure 6c). The jet mass flow rate coefficient C_q is considered the flow control parameter and it is defined as a ratio between the jet and diffuser mass flow rates, and in the present investigations it is less than 1% in all controlled cases. Schematics illustrating the fluidic oscillating jet operation are shown in Figure 5b. The fluidic actuator has two inlets which cause the two air jets to interact in an unstable fashion and adhere to one side of the orifice exit before switching to the opposite side. A single prototype of the fluidic oscillating jet is also characterized on the bench, and its operation is further illustrated in Figure 5c, which shows schlieren visualization of the resulting jet, issuing in quiescent air. As this internal oscillation between the two end states repeats, the jets switching direction at the orifice manifests in the meandering jet evolution into the air, as clearly seen in Figure 5c. This oscillation of the jet enhances the mixing with surrounding air and rapidly spreads the domain affected by the jet.

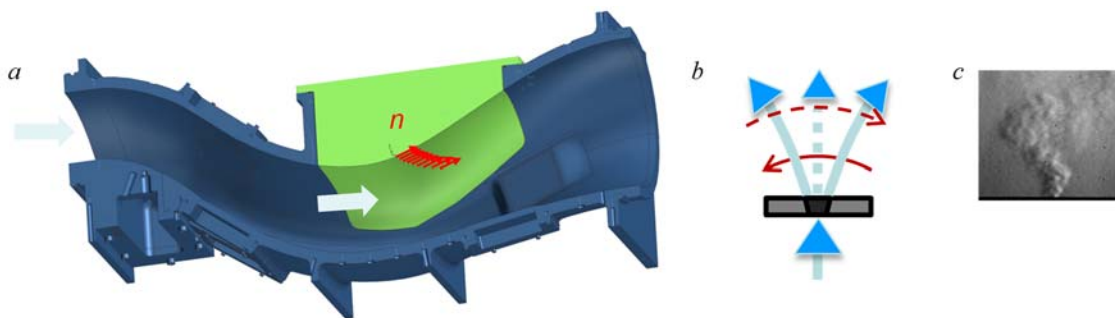


Figure 5. Schematics of the fluidic oscillating jet integration into the flow control module (a), a jet operation (b), and its schlieren visualization (c).

III. The Base Flow

Some structural details of the base flow (in the absence of actuation) are characterized using surface oil visualization at the nominal tunnel Mach number of $M_t = 0.64$, where a mixture of linseed oil and titanium dioxide paint is adjusted for the surface shear. The respective characteristic features of the topology of the separated base flow at the upstream and downstream turns of the diffuser are shown in Figures 6a and b

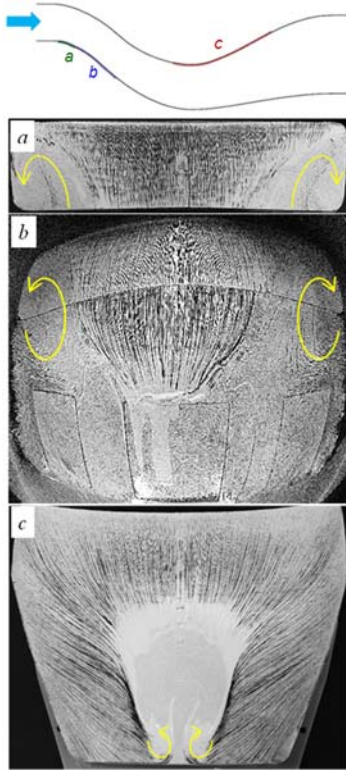


Figure 6. Surface oil-flow visualization on the duct surface at $M_t=0.64$ for the incipient (a), full upstream (b) and downstream (c) flow separation. Flow is top to bottom.

(bottom surface) and in Figure 6c (top surface). The images of oil streaks over the upstream surface in the absence of flow actuators (Figure 6a and b) show the onset of separation at each corner of the duct (the top edge of the image). The spanwise width of the centrally-attached flow (nearly symmetric about center span) that is marked by uninterrupted oil streaks diminishes in the streamwise direction, and the flow becomes fully spanwise separated at about 1/3 of the height of the image from the downstream end, such that the separation line forms an upstream-open horseshoe (Figure 6b). The oil streaks clearly show the presence of counter-rotating circulating flow at the spanwise edges (marked by arrows) that indicate coupled interaction with the counter-rotating streamwise vortices that form at the corners of the duct and persist through the AIP. This separation pattern indicates highly three-dimensional nature of the upstream flow separation that arguably leads to some upwelling of low-speed fluid from the bottom surface towards the diffuser's core and enhanced flow mixing farther downstream, as shown in the total pressure distortion at the AIP in Figures 1 and 7g. A second closed separation domain is present downstream of the second duct bend (Figures 6c), where a spanwise-compact local separation bubble is formed symmetrically about the diffuser's (center) plane over about a third of the span. The oil streaks mark not only the spanwise edges of separated domain, but also indicate that it is bounded by strong streamwise vortices (the downstream edge of the bubble is captured in Figure 6c). The oil traces shown in Figure 6c are utilized for placement of the jet actuator array, which is aligned with the upstream edge of the separation bubble.

Base flow distortions are characterized by the total-pressure rake measurements at the AIP for a range of diffuser Mach numbers $M_t = 0.32 - 0.69$, and the corresponding contour plots are shown in Figure

7. As already discussed in connection with Figure 1, there are two primary regions of total pressure deficit, centered about the top and bottom surfaces that are clearly related to the secondary flows induced by the internal separation at the diffuser's bends. As the Mach number is increased, the total pressure deficit spreads within the AIP indicating advection of low-momentum fluid from the wall region into the core flow by the secondary flow that is coupled to the flow separation. It is noted above, the distortion associated with the lower surface separation (near the throat) is somewhat more diffused compared to that arguably associated with top surface pair of counter-rotating vortices seen in Figure 6c. This difference may be

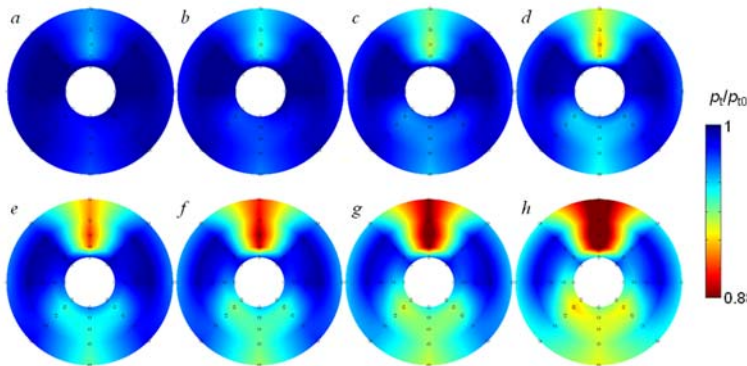


Figure 7. AIP base flow total pressure contour plots at $M_t=0.32$ (a), 0.37 (b), 0.43 (c), 0.48 (d), 0.54 (e), 0.59 (f), 0.64 (g), and 0.69 (h).

attributed to the opposite characteristics of the separation domains. While the upstream separation begins at the outboard edges of the bottom surface, the upstream separation is centrally symmetric about the center plane resulting in stronger, more coherent secondary motions that ultimately give rise to the pair of streamwise vortices. In fact, the total pressure distortion near the top surface of the AIP in Figure 7 is similar to the distortion that is brought about by

thick boundary layer ingested in an offset diffuser in the absence of internal flow separation (Gissen et al. 2014). This flow distortion pattern suggests that the streamwise vortices that are formed as a result of the interaction of the separation bubble with the corner flow in the present diffuser, and by the contraction of the incoming boundary layer vorticity when the inlet flow is contracted at the aperture are similar and lead to similar distortion patterns by advecting low momentum flow from the surface towards the AIP center. The oil visualization and the total pressure contours at the AIP indicate that as the separation domain becomes reattached, the vortex pair peels off the surface and migrates towards the centerline (Figure 6c).

Further insight into the structure of the base flow is provided by analysis of the static wall pressure distributions for the same range of diffuser Mach numbers. Two spanwise and two streamwise distributions of the pressure coefficient $C_p = 2 \cdot (p/p_r - 1) / (\kappa \cdot M_r^2)$ are shown in Figure 8 (the reference static pressure and Mach number are measured at the AIP face). The upstream set of spanwise pressure ports is located at $x/H = 3.3$, and spans $-1.3 < y/H < 1.3$ about the centerline. The family of pressure profiles at this location is shown in Figure 8a, indicating the flow symmetry about the central plane upstream of the separation, where the peak flow acceleration is along the centerline. The corresponding spanwise static pressure distributions at $x/H = 5.1$ ($-0.9 < y/H < 0.9$) across the separation bubble are shown in Figure 8b. The central three ports are contained within the bubble, showing the nearly uniform pressure at all flow condition, while the neighboring pressure dip indicates some flow acceleration just outside of the bubble, presumably due to the evolution of the streamwise vortices. The outboard pressure distributions indicate relative deceleration of the flow moving away from the streamwise vortices. Streamwise pressure profiles along the lower diffuser surface in Figure 8c indicate that the flow enters the diffuser throat ($x = 0$) with the highest velocity and immediately begins to decelerate along the lower surface, up to the pressure apex, just before $x/H = 4$, which coincides with the beginning of the second diffuser turn. As the lower diffuser surface guides the flow into second turn, the flow begins to accelerate and, consequently, the pressure decreases. The evolution of the pressure along the upper diffuser surface (Figure 8d) is markedly different, owing to the fundamental differences between the two internal separation patterns. An initial pressure increase between the first two pressure ports is followed by a sharp decrease up to the next pressure port, just past $x/H = 2$. As the flow approaches the second turn along the upper surface ($x/H < 4$), there is small net pressure increase, which is followed by significant adverse pressure gradient that leads to the local flow separation. The two pressure ports about $x/H = 5$ (upstream of the last two ports) are contained within the separated bubble and indicate that the pressure is leveling. Once the flow reattaches, the last two ports indicate flow spreading by the diffuser.

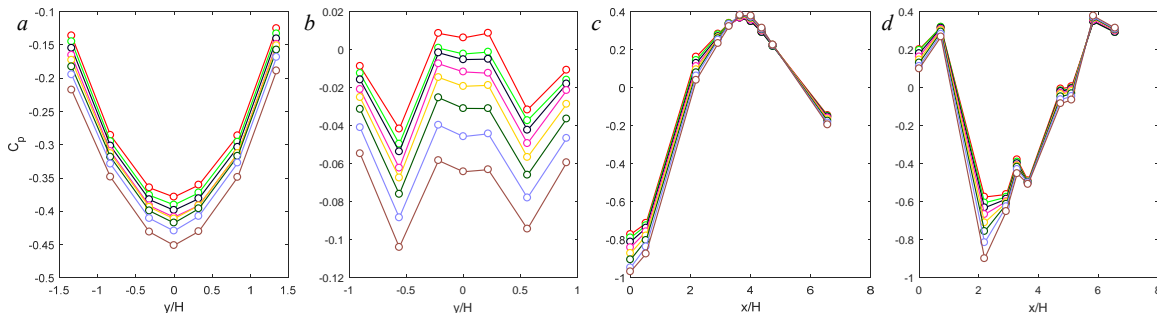


Figure 8. Base flow spanwise at $x/H=3.3$ (a) and 5.1 (b), and streamwise at the bottom (c) and top (d) wall centerline C_p profiles for $M_t=0.32$ (\circ), 0.37 (\circ), 0.43 (\circ), 0.48 (\circ), 0.54 (\circ), 0.59 (\circ), 0.64 (\circ), and 0.69 (\circ).

Some additional details are provided by color raster plots of surface pressure distributions obtained using pressure-sensitive paint (PSP) over the flow control insert (cf. Section II) for $0.37 < M_t < 0.64$, and shown in Figure 9. The (inactive) array of the jet orifices and the spanwise array of static pressure ports (cf. Figure 8b) are clearly visible in each of the images. As expected, the surface pressure globally decreases with increasing diffuser Mach number, but more importantly, pressure variations across the surface can be related to the flow features. Although the static wall surface ports shown in Figure 8a are outside of the PSP domain, the same trend of the upstream pressure distribution is captured by the PSP in Figure 9, namely, the oncoming flow upstream of the flow control jets induces a suction peak at the centerline, with

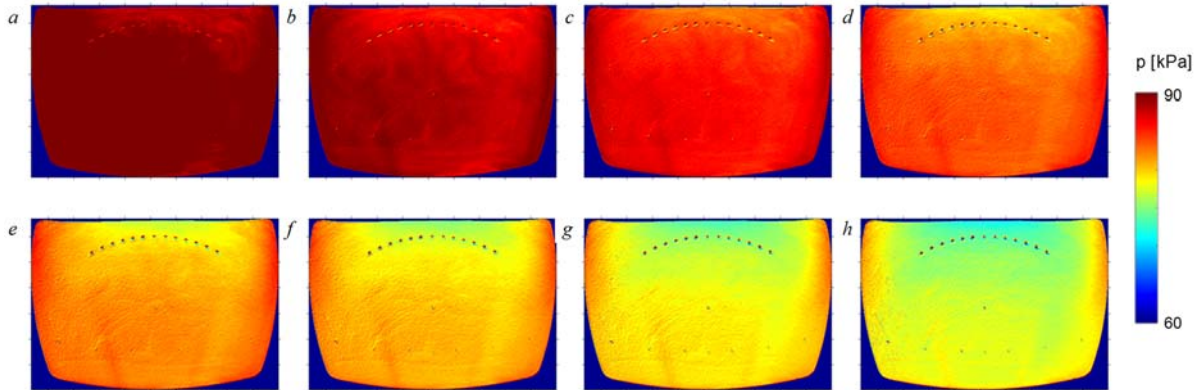


Figure 9. PSP-measured base flow pressure contour plots at $M_t=0.37$ (a), 0.43 (b), 0.48 (c), 0.54 (d), 0.56 (e), 0.59 (f), 0.61 (g), and 0.64 (h).

the pressure increasing outward from the center plane. The separation bubble downstream from the jet array is depicted by a region of elevated static pressure, and its spanwise bounds are marked by the highest pressure levels, which is related to the streamwise vortices along the spanwise edges of the bubble (cf. Figure 6c), in agreement with the direct spanwise pressure measurements at $x/H = 5.1$ (Figure 8b). Also in accord with the directly-measured spanwise pressure profiles in Figure 8b, a drop in the surface pressure just outside of the bubble bounds, and its rise further outbound is clearly captured by the PSP measurement technique.

IV. Flow Control Effects

As indicated previously by Figures 1 and 7, the distortion at the AIP is predominantly a result of the presence of the closed separation domain within the second turn of the diffuser and its coupling to the streamwise vortices. A crucial element of the present investigation is the use of active flow control (AFC) for deliberate manipulation of the trapped vorticity within the separation region and its coupling to the secondary vortices. Initially, actuation is provided by a spanwise array of $n = 17$ fluidic oscillators that is integrated into an insert in the diffuser's wall just upstream of the separation bubble. The effects of the actuation on the separation domain and on the total pressure distribution measured at the AIP are shown in Figure 10 for $M_t = 0.64$ (the base flow is shown for reference in Figure 10a). The actuation is applied at several levels of the mass flow rate coefficient C_q (relative to the total diffuser flow), ranging from $C_q = 0.07\%$ (Figure 10b) to 0.61% (Figure 10j). It should be noted that the flow control, being placed on the top side of the diffuser inner surface, is designed for mitigation of only the most prominent total pressure deficit concentrated about the upper AIP surface. Face-averaged circumferential distortion parameter $DPCP_{avg}$ for the considered base flow (Figure 10a) yields 0.038, predominantly due to the upper high pressure deficit region.

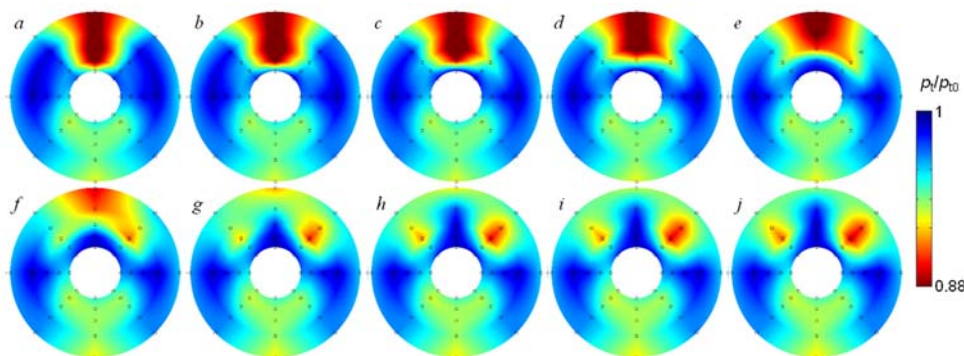


Figure 10. AIP total pressure contour plots at $M_t=0.64$ and $C_q=0\%$ (a), 0.07% (b), 0.14% (c), 0.20% (d), 0.27% (e), 0.34% (f), 0.40% (g), 0.47% (h), 0.54% (i), and 0.61% (j).

applied at the lowest C_q levels (Figures 10b – d), there is a weak proportional flattening of the total pressure deficit along the upper AIP surface that reduces the $DPCP_{avg}$ parameter by about 10%. As the C_q increases past 0.3% (Figure 10f), in addition to further

suppression of the deficit signature, its shape appears to begin to break. By $C_q = 0.4\%$ (Figure 10g), instead of a connected deficit domain, there is a small remainder of the original domain right at the top wall, while the two new small nodes emerge at about 45° on either side of the top surface. With the further increase in C_q (Figures 10h – j), the high momentum flow penetrates deeper into the central top region (e.g., compare the central top wall between Figures 10g and j), but the low momentum flow becomes increasingly concentrated into two nodes in the top central right and left positions of the AIP pressure contour. Therefore, there are the two competing effects of further deficit decrease in the central region and increasing deficit at the nodes. Overall, significant suppression of the distortion in the central region, and increase in the distortion in the side lobes due to the application of the flow control results in the aforementioned total pressure distortion reduction in about 50%, expressed through the $DPCP_{avg}$ parameter.

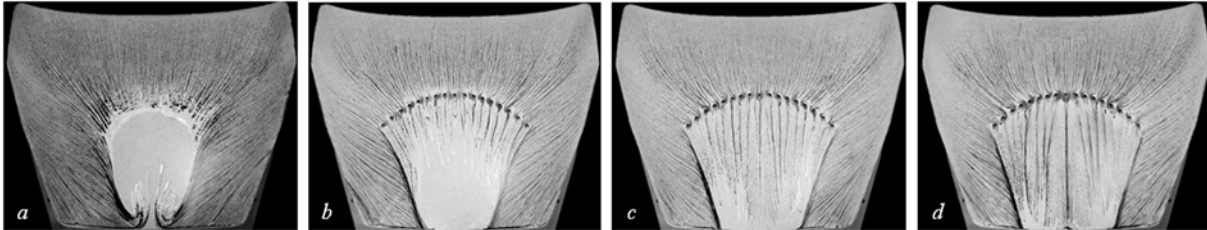


Figure 11. Surface oil-flow visualization over the downstream flow control insert, with full control array of $n = 17$ jets and flow control parameter $C_q = 0$ (a), 0.14% (b), 0.27% (c), and 0.41% (d) at $M_t = 0.64$.

To assess what changes to the flow are effected by the flow control jets, which result in observed the AIP total pressure changes, three flow control cases shown in Figure 10 are further examined by surface oil-flow visualization. Figure 11a shows the base flow visualization for reference, and the three characteristic controlled cases for $C_q = 0.14\%$, 0.27%, and 0.41% are shown in Figures 11b – d, respectively. At $C_q = 0.14\%$ (Figure 11b), the oil streaks show clear imprints of the streamwise vortices formed by each of the jets immediately downstream of the jet orifices. The actuation appears to delay the onset of separation (as is evidenced by the oil streaks), but the downstream end of the closed separation domain migrates farther downstream out of the field of view. Although the actuation does not seem to affect the strength of the streamwise vortices, it appears that they are slightly displaced laterally. This slight displacement is weakening the central upwash of the low momentum fluid that results in the weak flattening of the total pressure deficit seen in Figure 10c. The strong distortion at the upper segment of the AIP is still present even at $C_q = 0.27$ (Figure 10e), although the jets are able to maintain the attached flow further into the separation bubble, as seen in Figure 11c. A clear displacement of the streamwise vortices outward from the center is also associated with this C_q , which further diminishes the central upwash. Finally, at $C_q = 0.41\%$ (Figure 11d), the flow appears to be attached within the entire central domain over the second turn and this leads to weakening of

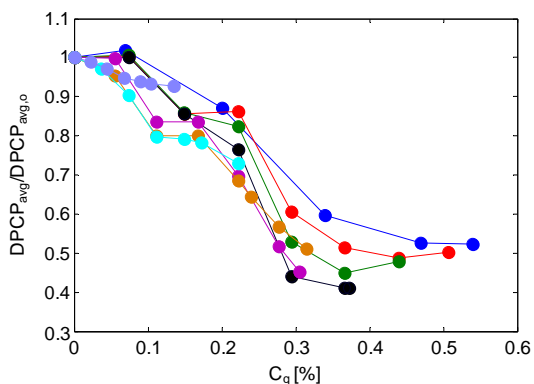


Figure 12. Relative change in the mean circumferential distortion Parameter $DPCP_{avg}$ with the jet mass flow ratio C_q for the control with $n = 3, 5, 7, 9, 11, 13, 15,$ and 17 jets ($M_t = 0.64$).

and even larger spanwise spacing between the secondary vortices, which in turn significantly diminishes the central total pressure deficit (Figure 10g), but creates two disparate nodes of the total pressure deficit, which are attributed to the eventual liftoff of the displaced streamwise vortices.

Following the demonstration of the effectiveness of the full ($n = 17$) jet array, an optimized jet configuration was sought by a stepwise decrease of the number of active central jets. This optimization study was in particular motivated by the finding that, past the certain total C_q level for the default jet array ($n = 17$), there was a trade off in further improvements due to the opposing trends that were discussed in Figure 10. Starting with the full jet array, two outermost jets are excluded from the active array, yielding actuation cases with 17 jets down to 3

central active jets, in increments of two. All of these actuation cases are tested with a varying C_q and their effectiveness is estimated by quantification of the AIP distortion by $DPCP_{avg}$ parameter. Figure 12 shows a relative change in the distortion parameter for all the cases that are tested. Several interesting features can be observed in the $DPCP_{avg}$ variation relative to n and C_q . First, initial flow response to small C_q improves with reduction of the number of jets; only five active jets are capable of a 20% reduction in distortion and only $C_q = 0.1\%$. This trend emphasizes the importance of the local jet effect, where for a given C_q , the local effect expressed through C_q/jet increases with decreasing number of jets. However, there is a plateau of how much distortion management can be done with a fixed number of jets, which precludes utilization of low- n actuation cases. For instance, the $n = 3$ case cannot effect more than 10% improvement, while $n = 5$ plateaus at less than 30% improvement. When examined for the optimal configuration, Figure 12 indicates that there is not necessarily a sharp cutoff that points to an optimal n . These results suggest that somewhere between $n = 9 - 13$ is a probable optimum, and that more parameters should be used for further narrowing of an optimum. A broad optimum is beneficial for any practical application, allowing for a wider operational range that would result in a significant distortion suppression. Furthermore, these initial optimization results indicate that nearly 60% reduction in $DPCP_{avg}$ could be achieved with C_q of less than 0.4%, compared to nearly 40% reduction at about $C_q = 0.6\%$ for the default jet configuration.

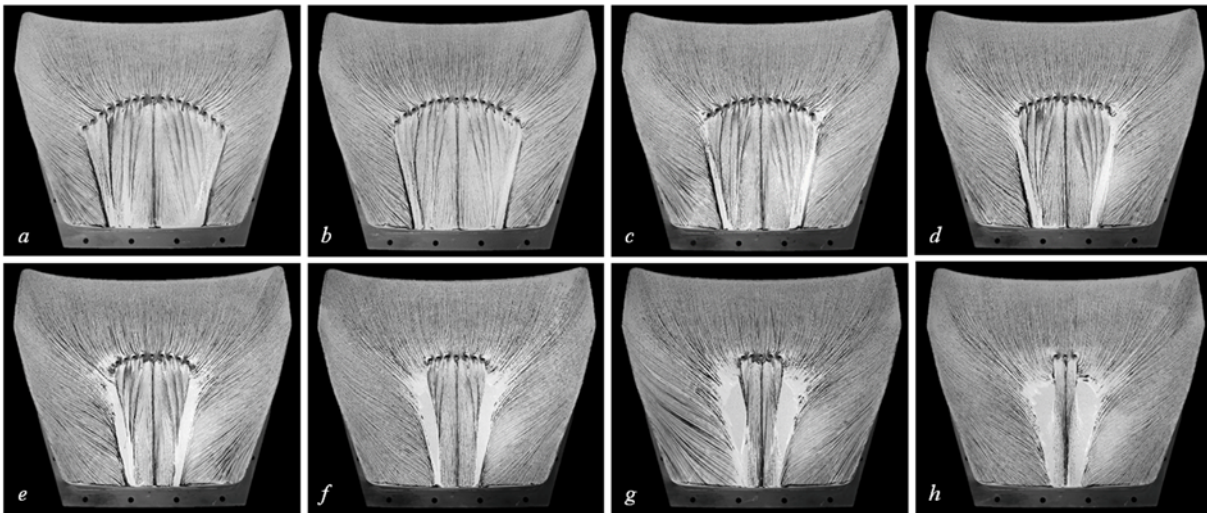


Figure 13. Surface oil-flow visualization over the downstream flow control insert, with flow control parameter $C_q = 3.2 \times 10^{-4}$ per jet and varying number of active jets $n = 17$ (a), 15 (b), 13 (c), 11 (d), 9 (e), 7 (f), 5 (g), and 3 (h) at $M_t = 0.64$.

Effect on the flow of these jet arrays with reducing number of active jets are examined with oil-flow visualization over the flow control surface, which is shown in Figure 13. These visualizations clearly show that, regardless of the number of active jets, the effect of the full jet array is maintained downstream of the active jets, when preserving C_q/jet , with the consequence that the spanwise extent of the attached flow narrows with the reduction in n . This also has a significant ramification on the spacing of the streamwise vortices that form along the boundary of the controlled and uncontrolled flow. They are furthest apart for the default $n = 17$ configuration, which was already discussed in Figure 11. As n decreases (Figures 13) another important feature becomes prominent. Already for $n = 13$ (Figure 13c), boundary between the controlled and uncontrolled flow widens, and the evolution of the flow in these boundaries gives rise to local streamwise separation cell that further spreads spanwise as the number of active jets decreases (see the boundary progression from Figure 13c to h). Each of these cells then has two close boundaries that each gives rise to a pair of streamwise vortices. These separation pockets, growing with a decrease in n , induce flow losses, which, combined with the decreasing separation between the streamwise vortices, leads to undesired synchronous sweeping of the low momentum fluid in between them. Therefore, reduction in

the number of active jets past the point at which the separation pockets grow induces not only favorable central flow reattachment, but also unfavorable streamwise vortex interaction.

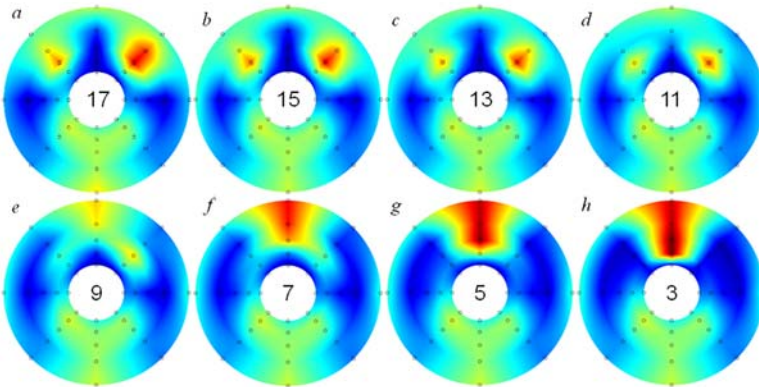


Figure 14. AIP total pressure contours labeled by the number of active jets at $M_t = 0.64$ and controlled by $C_q = 0.54\%$ (a), 0.47% (b), 0.41% (c), 0.35% (d), 0.28% (e), 0.22% (f), 0.16% (g), and 0.10% (h).

separation between them with a decrease in n , they still do not collocate and sweep the flow synchronously. However, as n is further reduced to $n = 9$ (Figure 14e), the vortex signatures diminish, while simultaneous increase in the total pressure deficit along the top wall is formed. It is argued that the separation between each pair of the streamwise vortices becomes insufficient to keep them apart past this array, and any further reduction in n (Figures 14f – h) does not prevent the vortex collocation, which increasingly sweeps the low momentum fluid towards the top wall, much like the base flow streamwise vortices. Although not as severe, structural distortion pattern for the three active jets (Figure 14h) does not differ much from the base pattern (Figure 10a). It should be noted, though, that the underlying flow dynamics of the base flow (governed by the two streamwise vortices detaching from the tail-end of the separation bubble, see Figure 6c) and that of the flow controlled by the three central jets (two pair of streamwise vortices forming along the interfaces between controlled and uncontrolled flow, Figure 13h) is substantially different.

Contour plots of the AIP total pressure that correspond to the flow visualization cases shown in Figure 13 are shown in Figure 14, establishing a connection between the jets effect on the flow and the resulting total pressure deficit at the AIP. As seen in each of the cases when $n = 17 - 11$ (Figures 14a – d) interaction between each pair of the streamwise vortices leads to their lift off the surface, thereby being displaced into the bulk flow, showing its signature as nodes of the total pressure deficit. Despite reducing

Although it is argued that a rather broad optimal configuration $n = 9 - 13$ can be inferred from the analysis shown in Figure 12, for the illustration purposes configuration $n = 13$ is selected for further investigation, as a representative of the optimization. Static pressure profile analogous to those shown in Figure 8 for the base flow are shown for $n = 13$ and $M_t = 0.64$ in Figure 15. Two sets of profiles for the two spanwise (Figures 15a and b) and streamwise (Figures 15c and d) pressure distributions are shown, corresponding to the uncontrolled and controlled flow cases which total pressure contours are shown in Figure 10a and 14c, respectively. Upstream spanwise pressure profiles (Figure 15a) indicate that although the flow control is applied downstream from this streamwise location, there is still a small favorable flow acceleration in the upstream flow, which is attributed to the somewhat reduced flow losses in the controlled flow. Downstream from the flow control array, spanwise profiles (Figure 15b) shown an increase in pressure across the board, as the controlled flow expands in the diffuser geometry, without the separation bubble that is present in the

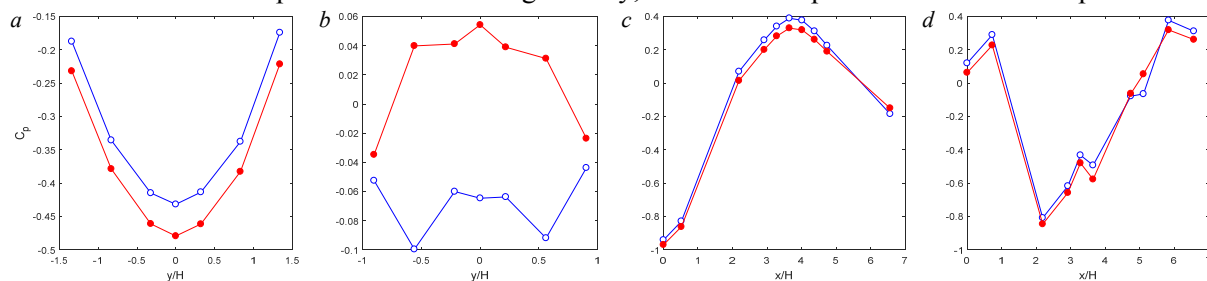


Figure 15. Spanwise C_p profiles at $x/H = 3.3$ (a) and 5.1 (b), and streamwise profiles along the bottom (c) and top (d) wall centerline, for $M_t = 0.64$, $n = 13$, and $C_q = 0\%$ (\circ) and 0.41% (\bullet).

base flow. Both the lower (Figure 15c) and upper (Figure 15d) streamwise pressure profiles show slight acceleration of the flow throughout the diffuser, while prominently bypassing a signature of the separated flow pressure leveling within the separation bubble (Figure 15d), as the static pressure continuously rises past the second diffuser bend in the controlled flow.

The effectiveness of the actuation using the selected optimal jet array ($n = 13$) is characterized over a range of C_q in terms of several distortion and recovery (Figure 16d) parameters at four Mach numbers $M_t = 0.48$, 0.54, 0.59, and 0.64 (Figure 16): circumferential face-averaged (Figure 16a), tip (Figures 16b) and hub (Figures 16c), and radial tip (Figure 16e) and hub (Figure 16f) distortions. These data show that the trends of variation with C_q are similar over the range of the tested Mach numbers. The circumferential face-averaged distortion, $DPCP_{avg}$, decreases with increasing C_q , to between 50 and 55% at $C_q = 0.44\%$, for all M_t (Figure 7a). The tip circumferential distortion $DPCP_t$ (Figure 16b) is nearly invariant with C_q until the evolution of the streamwise vortices in the base flow is altered (and partially suppressed) at higher C_q ; the corresponding variation of the radial tip distortion (Figure 16e) follows the same trend, although at lower magnitude. The initial sharp drop in the hub distortion $DPCP_h$ (Figure 16c) at low C_q is followed by a weak increase with C_q (to 0.3 and then remains invariant), while the radial equivalent (Figure 16f) is not detrimental for any of the operating parameters. The significant decrease in the averaged circumferential distortion is accompanied by a weak increase in recovery (Figure 16d).

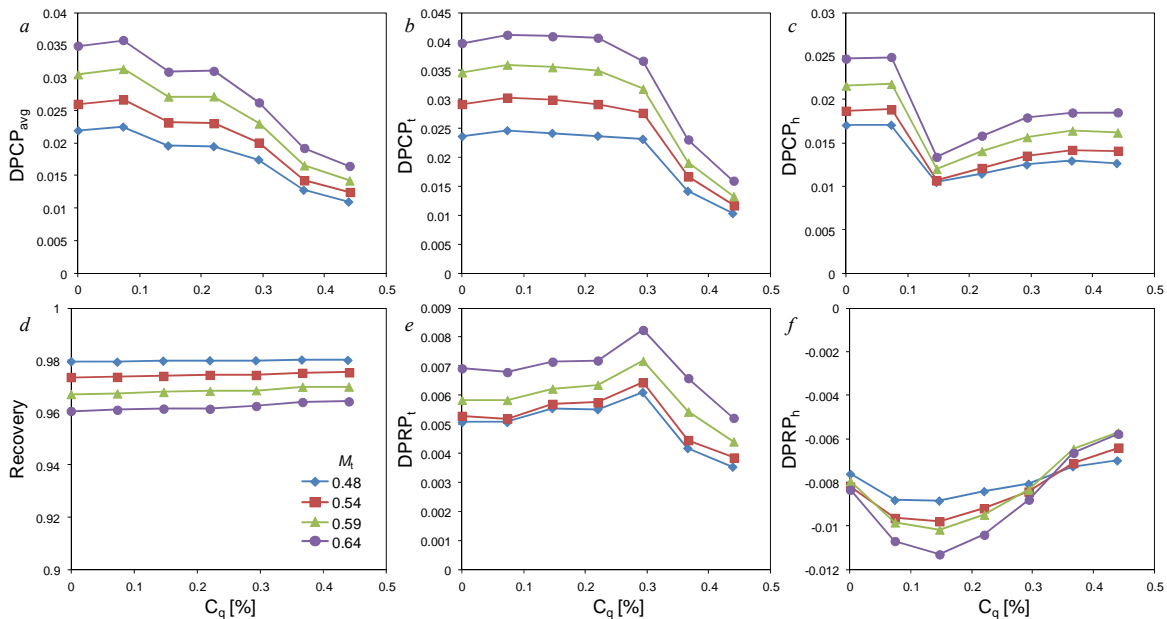


Figure 16. Distortion parameters $DPCP_{avg}$ (a), $DPCP_t$ (b), $DPCP_h$ (c), Recovery (d), $DPRP_t$ (e), and $DPRP_h$ (f) distributions with flow control parameter C_q for four M_t and optimized number of active jets ($n = 13$).

Finally, the resulting effects of actuation ($n = 13$) on the flow topology is investigated using PSP, as outlined in Section 2 and discussed with respect to the base flows in Figure 9. Contour plots of static pressure derived from the PSP measurements are shown in Figures 17 a and c, for the base and the flow controlled by $C_q = 0.41\%$, respectively. A camera used for PSP measurements is also utilized to record accompanying sets of surface oil-flow visualization for these two cases, such that direct comparison of the images can be made. Base flow features relating the weak pressure features with the bubble and streamwise vortices seen in the oil-flow visualization were already discussed in Figure 9. The pressure contour for the controlled flow (Figure 17c) indicates more prominent features of the controlled flow topology. First, the issuing jets

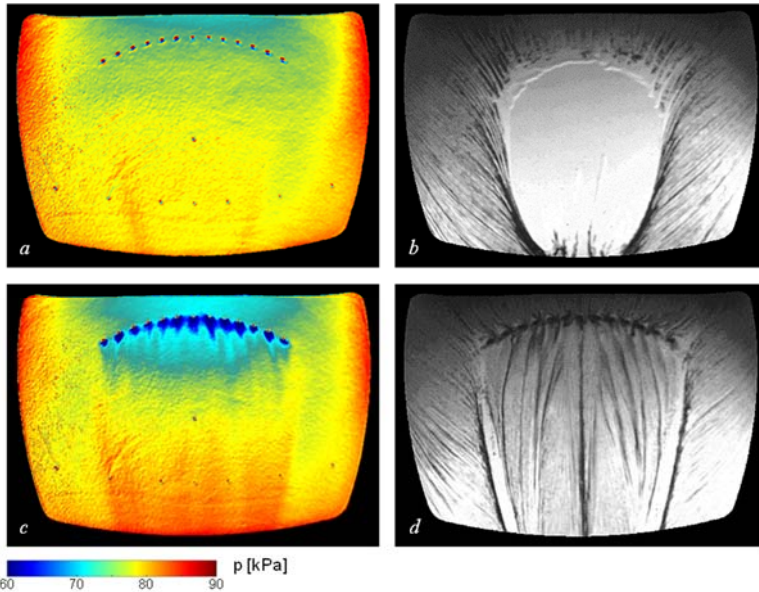


Figure 17. PSP-resolved contour plots of mean surface pressure (a, c) and the corresponding surface oil-flow visualizations (b, d) for the base (a-b, $C_q = 0$) and controlled (c-d, $C_q = 0.41\%$, $n = 13$) flows at $M_t = 0.64$.

are clearly marked by a localized low pressure region immediately downstream from the orifices. Moreover, even the flow upstream from the flow control array exhibits lowered surface pressure in the controlled flow, indicating accelerated flow, arguably due to the decreased diffuser flow losses. It is interesting to note that once the flow becomes attached over the base flow bubble, its surface pressure downstream from the initial jet interaction becomes increased relative to the base flow (Figure 17c). This surface pressure increase upon elimination of the separation bubble is related to the diffusing flow in the non-separated case, compared to the somewhat accelerated bulk flow above the separation bubble in the base flow.

V. Concluding Remarks

The present experimental investigations have focused on the application of active flow control to minimize losses and flow distortions in supersonic-inlet, aggressive offset diffusers for improved engine operability. Specifically, the primary objective of these investigations is to lessen recovery losses and flow distortions that are respectively effected by the closed separated flow domains on the concave surfaces of the diffuser's turns, and their dynamically coupled streamwise vortices. The current work has demonstrated that these secondary vortices are engendered by spanwise concentrations of streamwise vorticity that form in the outboard segments of the surface vorticity layer which bounds the separated flow domain. While separation induces losses that predominantly affect total pressure recovery, distortion results from the advection of low-momentum fluid from the wall region into the core flow by the streamwise vortices. The coupling mechanisms between the separation domains and the ensuing streamwise vortices are leveraged for significant reductions in flow distortion and losses. This is accomplished by using fluidic actuation based on a spanwise array of oscillating jets that is integrated into a downstream insert in the diffuser's wall just upstream of separation. These control jets alter the distributions and topology of trapped vorticity concentrations within the separated flow, thereby controlling the formation, evolution and intensification of the streamwise vortices.

The local and global characteristics of the diffuser flow in the absence and presence of actuation were investigated at throat Mach numbers up to $M_t = 0.64$ using a total pressure rake at the AIP, distributions of surface static pressure ports, and surface oil-flow visualization. The present investigations demonstrate that actuation by an array of surface actuation jets significantly modifies the structure and scale of the separated domain by inducing opposing sense vortices on each side of the span due to the spanwise-skewing of the jets, anti-symmetrically about center. Because of the coupling between the spanwise-compact separation past the second diffuser bend and the streamwise vortices in the base flow, the actuation effectively (and indirectly) controls the strength and structure of these vortices by inducing streamwise vorticity of opposite sense along each of the counter-rotating streamwise vortices. As a result, active flow control reduces the distortion at the AIP by up to 60% at $M_t = 0.64$ using mass flow rate ratio (actuation to diffuser flow) as low as $C_q \approx 0.4\%$, which is optimized by adapting the spanwise scale of the actuator array (and thereby

concentrations of streamwise vorticity) to the characteristic width of the separation domain using as few as two thirds of the available actuation jets.

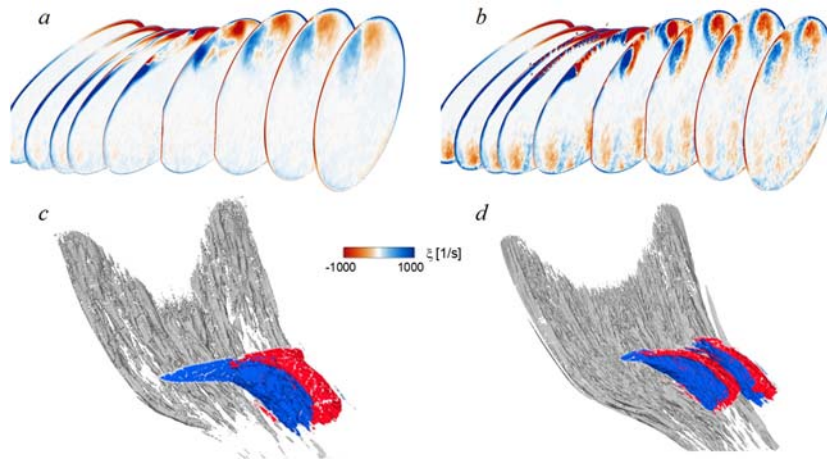


Figure 18. Simulations (Lakebrink and Mori, 2017) of the base (a, c) and controlled (b, d) flows ($n = 13$, $C_q = 0.41\%$) showing the evolution of cross sections of the counter-rotating vortex pair (a, b) and streamwise isosurfaces of vorticity (c, d).

The changes in the global structure of the diffuser flow that are brought about by flow control, are elucidated using joint, yet unpublished simulations at the Boeing company (Lakebrink and Mani, private communication) that illuminate the three-dimensional features of the flow field in the absence and presence of flow control. Figures 18a and b show color raster plots of streamwise vorticity within multiple diffuser cross sections normal to and along its centerline. The simulations of the base flow (Figure 18a) show that the

secondary counter-rotating vortices roll up from concentrations of streamwise vorticity of opposite sense that form within the outboard spanwise segments of the boundary layer outside the closed separated flow domain in the diffuser's second turn (CW in the left segment). The transport of low-momentum fluid from the upper surface by the vortex pair results in the significant total-pressure distortion in Figure 10a. In the presence of actuation ($n = 13$, $C_q = 0.41\%$, Figure 18b), the skewed off-center jets towards the side wall on each half of the span form predominantly single-sign streamwise vorticity (CCW on the left) of opposite sense relative to the streamwise vorticity that is already present in that spanwise half of the boundary layer (CW on the left). As shown in Figures 18c and d, the presence of the jet-induced opposite sense vorticity not only diminishes the separation, but also alters the rollup of each streamwise vortex and leads to significant spanwise displacement and weakening of its core, thereby improving both recovery and distortion at the AIP.

Acknowledgment

This work has been supported by ONR, monitored by Dr. Knox Millsaps.

References

- Anderson, B. H., and Gibb, J. "Study on Vortex Generator Flow Control for the Management of Inlet Distortion," *Journal of Propulsion and Power* Vol. 9, No. 3, 1993, pp. 422-430.
- Anderson, B. H., Mace, J. L., and Mani, M. "Active Fail- Safe Micro- Array Flow Control for Advanced Embedded Propulsion Systems - NASA/TM-2009-215596." NASA Glenn Research Center, 2009.
- Anderson, B. H., Miller, D. N., Addington, G. A., and Agrell, J. "Optimal Micro- Jet Flow Control for Compact Air Vehicle Inlets - NASA/TM-2004-212937." NASA Glenn Research Center, 2004.
- Anderson, B., Tinapple, J., and Surber, L. "Optimal Control of Shock Wave Turbulent Boundary Layer Interactions Using Micro-Array Actuation," *AIAA Paper 2006-3197*, 2006.
- Bell, J. H., Schairer, E. T., Hand, L. A., and Mehta, R. D. "Surface Pressure Measurements Using Luminescent Coatings," *Annual Review of Fluid Mechanics* Vol. 33, No. 1, 2001, pp. 155-206.
- Burrows, T. J., Gong, Z., Vukasinovic, B., and Glezer, A. "Investigation of Trapped Vorticity Concentrations Effected by Hybrid Actuation in an Offset Diffuser," *AIAA Paper 2016-0055*, 2016.
- Gartner, J. and Amitay, M. "Flow Control in a Diffuser at Transonic Conditions." *AIAA Paper 2015-2484*, 2015.
- Gissen, A., Vukasinovic, B., and Glezer, A. "Dynamics of Flow Control in an Emulated Boundary Layer- Ingesting Offset Diffuser," *Exp. Fluids* Vol. 55, No. 8, 2014, pp. 1-19.

- Gissen, A., Vukasinovic, B., McMillan, M., and Glezer, A. "Distortion Management in a Boundary Layer Ingestion Inlet Diffuser Using Hybrid Flow Control." *Journal of Propulsion and Power*, Vol. 30, 2014, pp. 834-844.
- Harrison, N., Anderson, J., Fleming, J., and Ng, W. "Active Flow Control of a Boundary Layer- Ingesting Serpentine Inlet Diffuser," *Journal of Aircraft* Vol. 50, No. 1, 2013, pp. 262-271.
- Jirasek, A. "Development and Application of Design Strategy for Design of Vortex Generator Flow Control in Inlets," *AIAA Paper 2006-1050*, 2006.
- Kavandi, J., Callis, J., Gouterman, M., Khalil, G., Wright, D., Green, E., Burns, D., and McLachlan, B. "Luminescent Barometry in Wind Tunnels," *Review of Scientific Instruments* Vol. 61, No. 11, 1990, pp. 3340-3347.
- Khalil, G. E., Costin, C., Crafton, J., Jones, G., Grenoble, S., Gouterman, M., Callis, J. B., and Dalton, L. R. "Dual-Luminophor Pressure-Sensitive Paint," *Sensors and Actuators B: Chemical* Vol. 97, No. 1, 2004, pp. 13-21.
- Lakebrink, M., and Mani, M., The Boeing Co, *Private Communication*, 2017.
- Liu, T., Campbell, B. T., Burns, S. P., and Sullivan, J. P. "Temperature- and Pressure- Sensitive Luminescent Paints in Aerodynamics," *Appl. Mech. Rev.* Vol. 50, No. 4, 1997, pp. 227-246.
- Owens, L. R., Allan, B. G., and Gorton, S. A. "Boundary-Layer-Ingesting Inlet Flow Control," *Journal of Aircraft* Vol. 45, No. 4, 2008, pp. 1431-1440.
- Peterson, J. I., and Fitzgerald, R. V. "New Technique of Surface Flow Visualization Based on Oxygen Quenching of Fluorescence," *Review of Scientific Instruments* Vol. 51, No. 5, 1980, pp. 670-671.
- Rabe, A. "Effectiveness of a Serpentine Inlet Duct Flow Control Scheme at Design and Off- Design Simulated Flight Conditions." Ph.D. Thesis, Virginia Polytechnic Institute, 2003.
- Reichert, B. A., and Wendt, B. J. "Improving Curved Subsonic Diffuser Performance with Vortex Generators," *AIAA Journal* Vol. 34, No. 1, 1996, pp. 65-72.
- SAE International. "Gas Turbine Engine Inlet Flow Distortion Guidelines." *Aerospace Recommended Practice 1420 Revision B*. 2011.
- Scribber, A., Ng, W., and Burdisso, R. "Effectiveness of a Serpentine Inlet Duct Flow Control Technique at Design and Off- Design Simulated Flight Conditions," *Journal of Turbomachinery* Vol. 128, No. 2, 2006, pp. 332-339.
- Tournier, S., Paduano, J., and Pagan, D. "Flow Analysis and Control in a Transonic Inlet," *AIAA Paper 2005-4734*, 2005.
- Vaccaro, J., Amitay, M., and Vasile, J. "Active Control of Inlet Ducts," *AIAA Paper 2008-6402*, 2008.
- Vakili, A., Wu, J., Liver, P., and Bhat, M. "Flow Control in a Diffusing S-Duct," *AIAA Paper 85-0524*, 1985.
- Vukasinovic, B., Burrows, T. J., Glezer, A., Lakebrink, M. T., and Mani, M. "Experimental and Numerical Investigation of Controlled Flow Distortion in a Subsonic Offset Diffuser by Trapped Vorticity," *AIAA Paper 2017-1454*, 2017.
- Weigl, H. J., Paduano, J., Frechette, L., Epstein, A., Greitzer, E., Bright, M., and Strazisar, A. "Active Stabilization of Rotating Stall and Surge in a Transonic Single Stage Axial Compressor," *ASME 1997 International Gas Turbine and Aeroengine Congress and Exhibition*, 1997, V004T15A034.